PERGAMON International Journal of Multiphase Flow 24 (1998) 1105–1138

International Journal of Multiphase Flow

Direct numerical simulation of droplet collisions in a turbulent channel flow. Part II: collision rates

M. Chen [a,*], K. Kontomaris [b], J.B. McLaughlin [a]

[a] *Department of Chemical Engineering, Clarkson University, Potsdam, New York, 13699-5705, USA*
[b] *DuPont Central Research and Development Experimental Station, Wilmington, Delaware, 19880-0304, USA*

Received 10 February 1997; received in revised form 2 February 1998

Abstract

Part I of this paper extended previous methods of particle tracking in Direct Numerical Simulations (DNS) of turbulence by allowing for inter-particle collisions. Part II employs these methods to investigate the early stages of evolution of mono-size suspensions of coalescing droplets, uniformly released in air. The droplet diameter was varied in the range 3 to 17 μm. The average collision rate in the channel core was found to be strongly dependent on the droplet inertia.

Keywords: Droplet collisions; Direct numerical simulations

1. Introduction

The algorithm documented in Part I was developed to study the evolution of the droplet size distribution of coalescing aerosols in turbulent flows. Part II of this work applies the new algorithm to study the early stages of evolution of monodispersed suspensions of droplets in a DNS of channel flow. The flow is assumed isothermal and it is driven by a constant mean pressure gradient. Although the mean flow is in the vertical direction, gravity effects for the types of droplets investigated in this paper were negligible. Fig. 1 of Part I shows the flow geometry. All results were obtained at a low Reynolds number (7050, based on the hydraulic channel diameter and the bulk average flow velocity.)

This work differs from recent related contributions (Sundaram and Collins, 1997; Hu and Mei 1997) in that it allows for additional complexities that are usually encountered in

* Corresponding author.

0301-9322/98/$19.00
PII: S0301-9322(98)00008-1

commercial practice. First, solid boundaries spontaneously generate turbulence in their vicinity and introduce flow inhomogeneities that significantly influence the particle behavior. Furthermore, simultaneous droplet dispersion, coalescence and deposition is simulated in this work. This allows direct observation of the coupling between the underlying phenomena and the evolution of the droplet size distribution.

A primary goal of this work was to determine the dependence on process variables of the average collision rate in a nearly monodisperse assembly of droplets dispersed in a given gas medium (air) in turbulent motion. This information is required when the evolution of the droplet size distribution is calculated from a population balance equation. By modeling only the details of individual particle collisions which are well understood from classical mechanics, the collective macroscopic behavior of the particle assembly can be realistically reproduced and studied.

For a given fluid, the interdroplet collision rate is expected to be a function of the flow Reynolds number and the properties of the droplet phase, namely droplet size, density and volume fraction (or, equivalently, number concentration or mass loading.) This study focused on droplets with diameters in the range 3 to 17 μm. Within this range, a transition is expected from the limit of "small" droplets which closely follow the motions of the surrounding fluid to a regime where the motion of "large" droplets correlates weakly with that of the fluid. Droplet densities 20 to 2000 times larger than the surrounding air were considered. Currently available computational capacity limited the scope of this work to dilute suspensions with initial droplet volume fractions, ϕ_0, in the range 5.84×10^{-6}–3.13×10^{-4}. The maximum bulk-average mass loading of droplets examined was 0.22. The droplet mass loading, m_l, was defined as the ratio of the average droplet mass flow rate to the gas mass flow rate.

At the low particle loadings considered in this paper, one might expect that the feedback effect of the particles on the gas turbulence would be negligible. However, Brooke et al. (1992), and Chen and McLaughlin (1995), have observed a considerable degree of instantaneous micro-segregation of particles (primarily in the vicinity of the channel walls) even at very low bulk-average particle loadings comparable to those considered in this paper. Particles tended to align along the well-known low-momentum streamwise streaks that have been associated with turbulence production. It is, therefore, possible that local particle accumulation may interfere with turbulence generation which would affect the global turbulence dynamics. However, in this paper, feedback effects were neglected.

In a typical run, a large number of droplets of a given size were released in the simulated channel flow at random positions according to a uniform distribution. At the time of the release, the channel flow was stationary and fully-developed. In the absence of particle feedback effects, it remained stationary and fully-developed for the duration of a run. Then, the evolution of the fluctuating three-dimensional gas flow field and the droplet trajectories were calculated for a prescribed length of time by integrating the governing equations of motion.

A number of factors complicate the interpretation of the observed collision rates. The number of droplets in the channel gradually decreases due to deposition. Furthermore, the initially uniform droplet concentration is skewed due to the preferential accumulation of droplets in the viscous wall region driven by the turbulence dynamics. Moreover, droplet coalescence leads to the formation of larger droplets whose mass is some integer multiple of

the mass of the originally released droplets. Finally, the properties of the turbulence vary with distance from the channel walls.

Over the range of conditions of interest in this work, the mean time between collisions, τ_c, was considerably smaller than the time, T_d, needed for a substantial depletion of droplets from the channel core due to wall accumulation and deposition. Furthermore, in the early stages of evolution (i.e. times not too large compared to τ_c), only a small fraction of the originally released particles coalesce to form larger ones. Therefore, for observation times between τ_c and T_d, a uniformly released monodisperse droplet suspension is expected to reach a pseudo-stationary collision rate in the nearly homogeneous isotropic part of the flow in the channel core, which can be associated with the original droplet size and concentration.

The primary focus of Part II of this paper is the determination of average collision rates in the channel core, although the complex effects of flow inhomogeneity and wall segregation are also reported. The flow in the core of the channel was approximately homogeneous. The degree of anisotropy in the core was previously discussed by Kontomaris and Hanratty (1994). The Reynolds number, Re_λ, at the channel centerline based on the Taylor microscale and the turbulence intensity, averaged over the three coordinate directions, was 29.7.

Interdroplet collisions over the range of parameters examined in this paper are driven primarily by particle inertia. The contribution of Brownian motion was negligible. Also negligible was the effect of gravitational forces; therefore, the results are directly applicable to horizontal flows. Average collision rates in the channel core are reported and interpreted in the context of the small and large particle limit theories of Saffman and Turner (1956) and Abrahamson (1975), respectively. Observed collision rates were between the limiting theoretical predictions. The droplet relaxation time was found useful in correlating collision rates. It appeared that the asymptotic expressions were in agreement with the observed trends for small and large particles. However, a study over a wider range of particle sizes would be required to firmly verify the theoretical expressions and establish their range of applicability.

2. Interdroplet collisions: theory review

A useful theory of interparticle collisions would predict the average collision rate from known properties of the flow (e.g. Reynolds number and dissipation rate) and the particle phase (e.g. concentration, diameter, and density.) Existing theories apply only to idealized flow types and narrow ranges of conditions. Furthermore, the validity of their underlying assumptions and their range of applicability are not well established. The purpose of this section is to formally define statistical quantities that are used to describe collisions and to review existing theories.

Interparticle collisions can be driven by a number of mechanisms. Interest is here limited to monodisperse suspensions in isotropic turbulence. Beal (1972) has shown that Brownian motion makes a negligible contribution to the collision rate for particles with diameters larger than about one micron dispersed in a gas. Similarly, gravitational particle acceleration is expected to make only a negligible contribution to the collision rate between small particles of equal size considered in this paper.

The average number of collisions per unit time per unit volume, Z, in a monodisperse

particulate system can be expressed according to Sundaram and Collins (1997) as

$$Z = \frac{1}{2} g(d) C^2 A \bar{w}. \tag{1}$$

In Eq. (1), $g(d)$ is the particle radial distribution function at contact, related to the probability density function of the relative particle separation. It represents a correction to the local number density due to nonuniformities in the spatial particle distribution. The symbol C denotes the average number of particles per unit volume (or particle number concentration.) The effective cross-section, A, presented by a fixed particle to approaching particles is

$$A = \pi d^2 \tag{2}$$

for hard spheres of diameter d. The mean relative particle speed at contact is formally defined as

$$\bar{w} = \int w P(\mathbf{w}|\mathbf{d}) \mathbf{dw}, \tag{3}$$

where $w = |\mathbf{w}|$ and $P(\mathbf{w}|\mathbf{d})$ is the conditional probability density function at contact. The factor 1/2 is included to correct for double counting of collisions between identical particles.

Other physically illuminating descriptors of the collision process can be defined from the average collision rate, Z. A collision coefficient is defined as

$$z = \frac{Z}{C^2} \tag{4}$$

to express the relation of the collision rate to all variables other than the particle number concentration for which a quadratic dependence is expected. The collision frequency, defined as the number of collisions of a single particle per unit time, is given by

$$f_c = \frac{2Z}{C}. \tag{5}$$

Closely related is the mean free time defined as the mean time between two successive collisions of a single particle:

$$\tau_c = \frac{1}{f_c}. \tag{6}$$

The mean free path is the average distance traveled by a particle between two successive collisions; for homogeneous, isotropic turbulence it is related to the mean free time as

$$\lambda_c = \bar{v} \tau_c, \tag{7}$$

where $\bar{v}$ is the average speed of the particles in a frame of reference where the average fluid velocity vanishes.

Application of the above formulas for given particle concentration and diameter requires an evaluation of the particle average speed, $\bar{v}$, average relative speed at contact, $\underline{w}$, and the radial distribution function at contact, $g(d)$. Analytical evaluations are possible in the limits of particles at zero and infinite inertia.

Saffman and Turner (1956) examined the limit of particles much smaller than the Kolmogorov eddy with negligible inertia. Such particles completely follow the surrounding fluid motions and they collide due to the local spatial variations in the turbulent velocity. The relative motion of neighboring particles is governed by the small scales of turbulence which were assumed isotropic. Furthermore, derivatives such as $\partial u/\partial x$ were assumed to be normally distributed with a mean square value given by

$$\left(\overline{\frac{\partial u}{\partial x}}\right)^2 = \frac{\epsilon}{15\nu}, \tag{8}$$

where ϵ is the rate of fluid turbulence kinetic energy dissipation per unit mass and ν is the fluid kinematic viscosity. It follows (see the appendix) that the mean value of $\left|\partial u/\partial x\right|$ is

$$\left|\overline{\frac{\partial u}{\partial x}}\right| = \left(\frac{2\epsilon}{15\pi\nu}\right)^{1/2}. \tag{9}$$

(In the paper by Saffman and Turner, the factor of π in Eq. (9) is missing. Their final expression for the collision rate is correct.) The relative particle velocity was assumed proportional to $d\left|\partial u/\partial x\right|$.

The collision rate between identical droplets induced by turbulent shear was estimated by Saffman and Turner (ST) as

$$Z = \left(\frac{2\pi}{15}\right)^{1/2} C^2 d^3 \frac{1}{\tau_k} \approx 0.647 C^2 d^3 \frac{1}{\tau_k}, \tag{10}$$

where

$$\tau_k = \left(\frac{\nu}{\epsilon}\right)^{1/2}, \tag{11}$$

is the Kolmogorov time scale. A factor 1/2 is included in [10] to correct for double counting of collisions. Sundaram and Collins (1997) arrived at the same result starting from the general expression in Eq. (1). Both derivations required that the particles be randomly distributed [$g(d) \approx 1$] so that their position and the turbulence properties are completely uncorrelated. This is plausible for particles of negligible inertia in isotropic turbulence.

Abrahamson (1975) considered the limit of particles with large inertia. In this case, colliding particles originate from different eddies and have uncorrelated velocities. Abrahamson found

that, in isotropic turbulence, the collision rate takes the form

$$Z = 2\sqrt{\pi}C^2 2d^2(\overline{V^2})^{1/2} \approx 3.545C^2 d^2(\overline{V^2})^{1/2}, \tag{12}$$

where $(\overline{V^2})^{1/2}$ is the root-mean-square value of the fluctuations of any of the Cartesian components of the particle velocity:

$$(\overline{V^2})^{1/2} = u'_{\mathrm{p}} = v'_{\mathrm{p}} = w'_{\mathrm{p}}. \tag{13}$$

Abrahamson defined particle fluctuating velocities relative to the average velocity of the surrounding fluid.

Sundaram and Collins (1997) derived Eq. (12) from the general expression for the collision rate in Eq. (1). Their derivation again requires that the particle positions are randomly distributed which is plausible for particles of very large inertia in isotropic turbulence.

Flow in the core of a channel is only approximately isotropic. In applying Abrahamson's expression, a directionally averaged particle turbulence intensity is used; it is defined by

$$\overline{V^2} = \frac{1}{3}(u_{\mathrm{p}}^{'2} + v_{\mathrm{p}}^{'2} + w_{\mathrm{p}}^{'2}), \tag{14}$$

where u'_{p}, v'_{p} and w'_{p} are the root-mean-square values of the x, y, and z components of the particle velocity fluctuations.

Abrahamson related the particle turbulence intensity, $(\overline{V^2})^{1/2}$, to that of the fluid, $(\overline{U^2})^{1/2}$. For homogeneous, isotropic flows, he suggested that

$$\overline{V^2} = \frac{\overline{U^2}}{\left(1 + \frac{1.5\tau\epsilon}{U^2}\right)}, \tag{15}$$

where τ is the particle relaxation time. In the core of the channel flow, the mean square turbulence intensity for the fluid is defined as

$$\overline{U^2} = \frac{1}{3}(u^{'2} + v^{'2} + w^{'2}), \tag{16}$$

where u', v' and w' are the root-mean-square values of the x, y, and z components of the fluid velocity fluctuations. For particles with sufficiently small relaxation times, Eq. (15) gives

$$\overline{V^2} \approx \overline{U^2}. \tag{17}$$

Abrahamson's theory relies on the assumption that the velocities of colliding particles are statistically independent. He estimated that this assumption was valid when

$$\frac{d^2}{5\mu\overline{U^2}/(\rho_{\mathrm{p}}\epsilon)} > 1. \tag{18}$$

Provided that this inequality is satisfied, one might expect the theory to be a reasonable

approximation in the core of the channel where the gradient of the mean flow is small. Abrahamson's theory should overpredict the collision rate for particles with finite relaxation times, since their velocities will have some correlation with the velocities of the fluid.

Williams and Crane (1983) presented a theory for collisions between particles with finite inertia. Their theory is considerably more complex than the Saffman–Turner theory and the Abrahamson theory. Since the latter theories provide a useful way of correlating the computed collision rates, the Williams–Crane theory will not be discussed further.

3. Results

The motivation for developing the methods described in the previous sections was the investigation of the phenomena that influence the long-term evolution of the particle size distribution in turbulent aerosol reactors. Their application in this paper, however, is limited to the early stages of droplet growth. The envelope of conditions examined was outlined in Tables 2–4 in Part I. This section describes the behavior of uniformly released monodisperse suspensions of droplets under isothermal conditions over the first 100 wall time units after their release. [Droplets with $\tau^+ = 50$ (Run 23) were traced for 300 wall time units.] A statistical characterization of key state variables is documented and insight into influential phenomena is sought. Particular attention is paid to phenomena pertinent to the interpretation of average interdroplet collision rates which is undertaken in the following section. All results are presented in wall units.

3.1. Gas turbulence

In all of the simulations in this paper, the effect of particle feedback on the carrier gas phase turbulence was neglected. This is a plausible approximation for dilute suspensions of very small particles especially in the early stages of dispersion from a uniform initial distribution before any significant particle accumulation in the wall region. Under these conditions, previous investigations of single-phase turbulent channel flow provide a thorough characterization of the underlying turbulence kinematics and dynamics.

The structure and Eulerian statistical properties of stationary, fully-developed, isothermal, single-phase turbulent channel flow have been extensively studied in the literature both experimentally and computationally. References to these studies may be found in Kim et al. (1987) and Lyons et al. (1991). Results for the low Reynolds number simulation (7050) that was used in the work have been thoroughly documented in Lyons et al. (1991). Fig. 1 reproduces the turbulence intensity profiles that are needed for the interpretation of collision rates. The values in Fig. 1 where obtained by averaging the corresponding quatities on the grid points of a given y^+ plane.

ST used the rate of turbulence dissipation to estimate the relative motion of small colliding particles. Fig. 2 shows the profiles of the average rate of dissipation of turbulent kinetic energy per unit mass of fluid and the mean-square values of the six components of the rate-of-strain

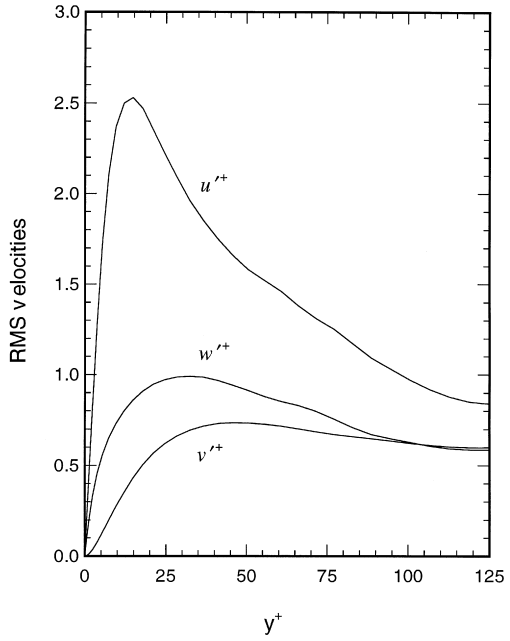

Fig. 1. Turbulence intensities of the numerical channel flow ($Re = 7050$).

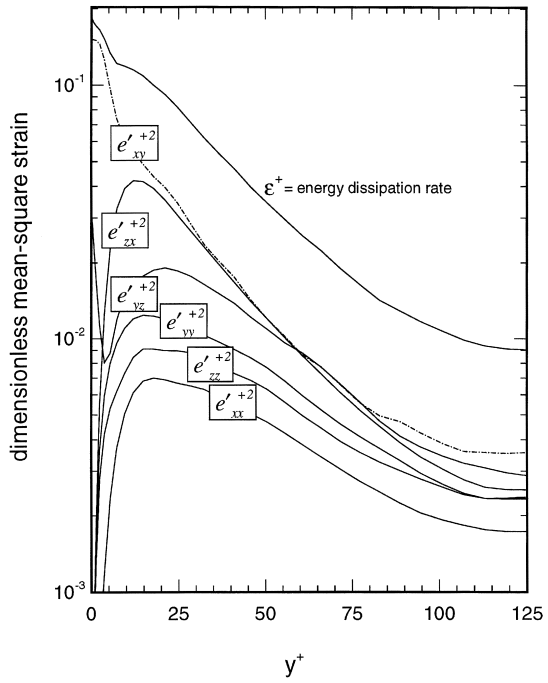

Fig. 2. The mean-square strain rate components and the average energy dissipation rate of the numerical channel flow ($Re = 7050$).

tensor. The dimensionless, local, instantaneous strain rate components were calculated as follows:

$$e_{xy}^{+} = \frac{\partial u^{+}}{\partial Y^{+}} + \frac{\partial v^{+}}{\partial x^{+}} \tag{19}$$

$$e_{yz}^{+} = \frac{\partial v^{+}}{\partial z^{+}} + \frac{\partial w^{+}}{\partial y^{+}} \tag{20}$$

$$e_{xz}^{+} = \frac{\partial u^{+}}{\partial z^{+}} + \frac{\partial w^{+}}{\partial x^{+}} \tag{21}$$

$$e_{xx}^{+} = 2\frac{\partial u^{+}}{\partial x^{+}} \tag{22}$$

$$e_{yy}^{+} = 2\frac{\partial v^{+}}{\partial Y^{+}} \tag{23}$$

$$e_{zz}^{+} = 2\frac{\partial w^{+}}{\partial z^{+}}, \tag{24}$$

where Y^{+} is the dimensionless distance from the channel center in the normal direction. It varies from $-h^{+}$ to h^{+}. The local dimensionless dissipation rate, ϵ^{+}, was calculated as follows:

$$\epsilon^{+} = e_{xy}^{+2} + e_{yz}^{+2} + e_{xz}^{+2} + \frac{1}{2}(e_{xx}^{+2} + e_{yy}^{+2} + e_{zz}^{+2}). \tag{25}$$

The wall unit of dissipation is $\epsilon^{*} = u^{*4}/\nu$. The values in Fig. 2 for e_{xy}^{+2}, e_{yz}^{+2}, e_{xz}^{+2}, e_{xx}^{+2}, e_{yy}^{+2}, e_{zz}^{+2} and ϵ^{+} were obtained by averaging the corresponding quantities on the grid points of a given y^{+} plane.

The energy dissipation rate increases in the vicinity of the walls. In the viscous sublayer, the main contribution to the energy dissipation rate is from e_{xy}. In the turbulent buffer layer, the main contributors to the energy dissipation are e_{xy} and e_{xz}. The contribution of the diagonal strain rate components to the energy dissipation rate is small, especially in the wall region.

Figs. 3 and 4 show that there are significant variations in the local instantaneous dissipation rates throughout the flow domain. Fig. 3 shows contours of the energy dissipation rate in the x–z plane. In the wall region, high energy dissipation rates are associated with the high and low speed streaks. Fig. 4 shows contours of the energy dissipation rate in the y–z plane. Most of the energy dissipation occurs in the wall regions. Large energy dissipation rates in the center of the channel are associated with fluid moving away from the wall regions (ejections).

The theories of ST and Abrahamson are strictly applicable to isotropic turbulence. Kontomaris and Hanratty (1994) noted that their low Reynolds number simulation exhibited significant anisotropy even at the channel center. The isotropy of the small scales of motion

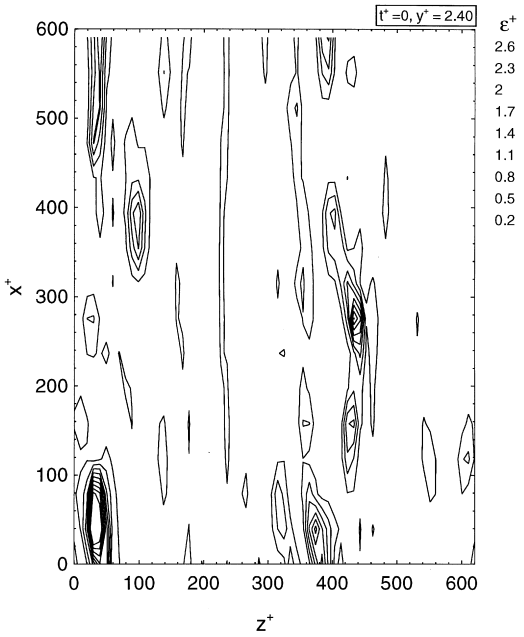

Fig. 3. Contours of the instantaneous energy dissipation rate at $t^+ = 0$ in the x–z plane at $y^+ = 2.4$.

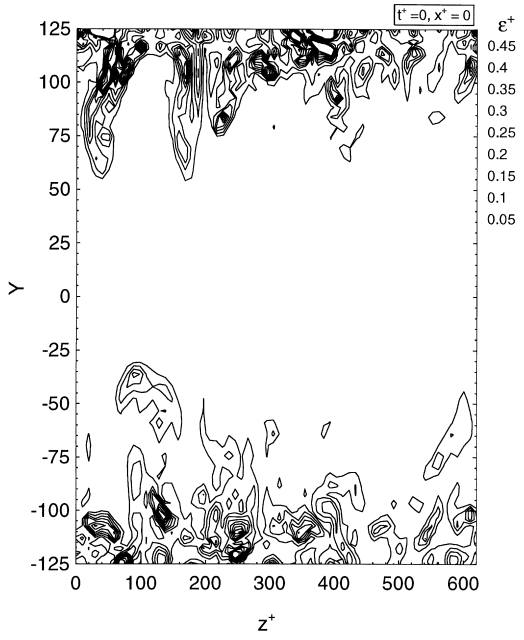

Fig. 4. Contours of the instantaneous energy dissipation rate at $t^+ = 0$ in the y–z plane.

can be quantified by the degree to which the following relation is satisfied:

$$\left(\overline{\frac{\partial u}{\partial x}}\right)^2 = \frac{1}{2}\left(\overline{\frac{\partial v}{\partial x}}\right)^2 = \frac{1}{2}\left(\overline{\frac{\partial w}{\partial x}}\right)^2. \tag{26}$$

In the low *Re* number simulation used in this work the mean-square values in the channel center of the velocity derivatives in the above equation were

$$\left(\overline{\frac{\partial u}{\partial x}}\right)^2 = 15.80\ \mathrm{s}^{-2}, \frac{1}{2}\left(\overline{\frac{\partial v}{\partial x}}\right)^2 = 14.20\ \mathrm{s}^{-2}, \frac{1}{2}\left(\overline{\frac{\partial w}{\partial x}}\right)^2 = 14.35\ \mathrm{s}^{-2}. \tag{27}$$

The degree of correlation between the velocities of approaching particles influences their collision rate. When the particle stopping distance is larger than the length scale of the largest turbulence eddies it might be expected that the velocities of approaching particles are uncorrelated. The velocities of small neighboring particles with stopping distances smaller than the Kolmogorov length scale of the surrounding fluid may be expected to be highly correlated.

Fig. 5 shows the variation of key turbulence length scales with distance from the wall. The Kolmogorov scale, η, was calculated from

$$\eta^+ = \left(\frac{1}{\epsilon^+}\right)^{1/4}. \tag{28}$$

Values for ϵ^+ were taken from Fig. 1. The dimensionless Taylor micro-scale was calculated as

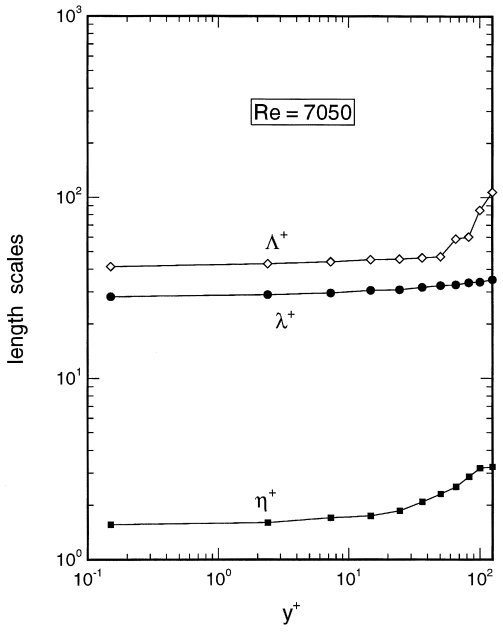

Fig. 5. Variation of the different length scales with distance from the closest wall.

follows:

$$\lambda^+ = \frac{1}{3}(\lambda_x^+ + \lambda_y^+ + \lambda_z^+), \tag{29}$$

where

$$\lambda_i^+ = \left(\frac{15(u_i'^+)^2}{\epsilon^+}\right)^{1/2}. \tag{30}$$

Values for the turbulent intensities were taken from Fig. 1. The dimensionless integral length scale, Λ^+, was calculated from

$$\Lambda^+ = \frac{1}{3}(\Lambda_{11}^+ + \Lambda_{22}^+ + \Lambda_{33}^+). \tag{31}$$

In Eq. (31), Λ_{ii}^+ is computed from integrals of the two point correlation functions, R_{ii} as follows:

$$\Lambda_{ii}^+ = \int R_{ii} \mathrm{d}x_i^+. \tag{32}$$

Fig. 5 shows that length scales in the core are larger than those in the wall region which agrees with intuition.

3.2. Droplet growth

Interdroplet collisions and coalescence produce droplets with masses that are equal to integer multiples of the masses of the originally released droplets. Fig. 6 shows the evolution of the cumulative size distribution of droplets with $S = 713$ for Run 16 which exhibited the largest collision frequency in this work. The weight percentage of the droplet mass remaining in suspension (i.e. non-deposited) at the end of the run ($t_f^+ = 100$) associated with droplets smaller than a given size is plotted against droplet cutoff size. Only singlets, doublets, triplets, and quartets are considered. The total dispersed mass resided with singlets at $t^+ = 0$. Fig. 6 quantifies the early droplet growth rate. It is seen that, at the end of 100 time wall units, more than 83% of the suspension still resides with singlets. Furthermore, it is shortly shown that the vast majority of droplets larger than singlets are found in the vicinity of the walls. This justifies the assumption that the suspension in the channel core remains nearly monodisperse and observed collision rates can be associated with the initial droplet size.

3.3. Droplet concentrations

The droplet concentration distribution influences the droplet collision and deposition rates and, therefore, the evolution of the droplet size distribution. In the early stages ($t^+ < 100$) of dispersion and growth from a monodisperse suspension, the suspension composition can be described in terms of only singlets, doublets, triplets, and quartets. The concentration of larger droplets is negligible. It is of interest to examine the early evolution of the average

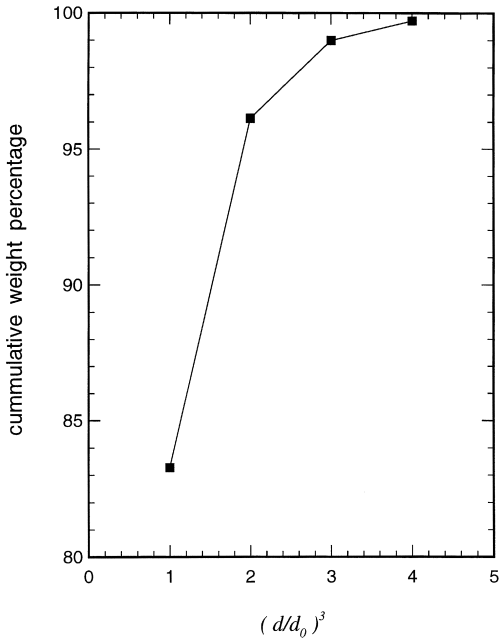

Fig. 6. Cumulative droplet size distribution after 100 wall time units for droplets with $S = 713$, $\tau^+ = 20$ (Run 16).

concentration profiles of low order multiplets. Deviations from average concentrations due to segregation of droplets in a microscopic scale are also of interest because they can affect collision rates.

3.3.1. Average droplet concentration profiles

Let $C_i(x,y,z,t)$ denote the locally ensemble or volumetrically-averaged number concentration for droplet size i, where $i = 1,2,3$ and 4 for singlets, doublets, triplets, and quartets, respectively. The total local concentration of droplets of all sizes is then given by

$$C_t(x, y, z, t) = \sum_{i=1}^{4} C_i(x, y, z, t). \tag{33}$$

The concentration of "specie" i, averaged over the homogeneous channel directions, is defined by

$$\overline{C_i} = \int_0^{L_x} \int_0^{L_z} C_i(x, y, z, t)\mathrm{d}x\mathrm{d}z/L_xL_z. \tag{34}$$

The total droplet concentration averaged over xz planes is then

$$\overline{C_t} = \sum_{i=1}^{4} \overline{C_i}(y, t). \tag{35}$$

A core-averaged concentration is defined by

$$\langle C_i\rangle_{\rm cr}(t)=\int_0^{L_x}\int_{-h+y_0}^{h-y_0}\int_0^{L_z} C_i(x,y,z,t)\mathrm{d}x\mathrm{d}y\mathrm{d}z/[2L_xL_z(h-y_0)], \tag{36}$$

where y_0 is the distance from the closest wall within which most of the variation of the concentration profiles is confined. For the conditions examined in this paper $y_0^+=30$. Again

$$\langle C_t\rangle_{\rm cr}(t)=\sum_{i=1}^{4}\langle C_i\rangle_{\rm cr}(t). \tag{37}$$

At the beginning of a typical run

$$\overline{C_1}^0=\overline{C_t}^0=\langle C_1^0\rangle_{\rm cr}=\langle C_t^0\rangle_{\rm cr}=C_0 \tag{38}$$

and

$$\overline{C_i}^0=\langle C_i^0\rangle_{\rm cr}=0,\quad i=2,3,4. \tag{39}$$

The evolution of the above concentrations is determined by droplet dispersion which leads to nonuniformities, droplet deposition which gradually depletes the channel, and coalescence which influences the populations of the different droplet multiplets. (Droplet resuspension from the wall and droplet breakup are not considered in this work.)

Fig. 7 shows the shape of the average concentration profiles of singlets, doublets and triplets at the end of Run 16, which exhibited the largest collision frequency in this paper. Each profile

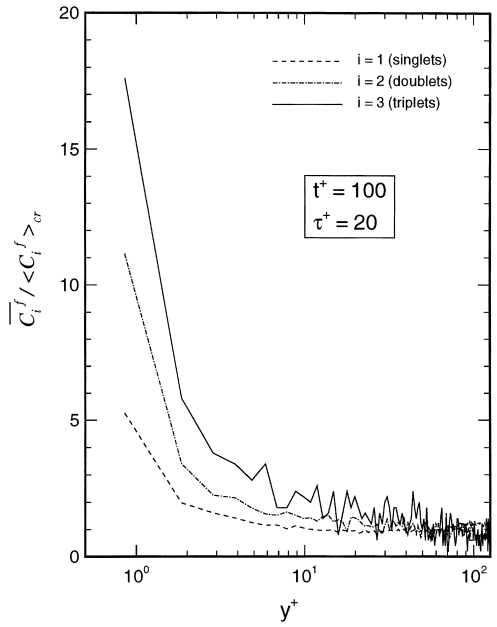

Fig. 7. The normalized concentration distribution of singlets, doublets and triplets at the end of Run 16.

Table 1
Core concentrations at the end of Run 16 ($t_f^+ = 100$, $\tau^+ = 20$, $C_0 = 1.26 \times 10^5$ cm^{-3})

i	$\langle C_i^f \rangle_{cr}$ cm^{-3}	$\langle C_i^f \rangle_{cr} / \langle C_1^f \rangle_{cr}$
1	1.00×10^5	1
2	6.30×10^3	0.063
3	6.30×10^2	0.0063
4	0	0

is normalized by the respective final core-averaged concentrations, $\langle C_i^f \rangle_{cr}$, which are given in Table 1, and it is averaged over both sides of the channel about its centerplane. Since no quartets were found in the core region at the end of the run, $\langle C_4^f \rangle_{cr} = 0$. As a result, the concentration of the quartets could not be normalized by the core-averaged concentration. The concentration profile of the quartets is not plotted in Fig. 7.

The initially statistically uniform distribution of singlets exhibits a strong segregation in the wall region after an elapsed time $t^+ = 100$. The maximum singlet concentration, $\overline{C_{1,max}}^f$, at $y^+ = 1$ is about 5 times its core value, $\langle C_1^f \rangle_{cr}$. Larger droplets created by coalescence also appear preferentially in the wall region where the maximum concentration of singlets is found. Profiles for all droplet sizes are approximately uniform for $y^+ > 30$. Table 1 shows that the final core concentrations of doublets, triplets and quartets remain negligible relative to the concentration of singlets. This justifies the assumption of a virtually monodisperse suspension in the channel core which simplifies the interpretation of collision rates. The core concentration of quartets is zero.

The effect of the droplet relaxation time constant on the shape of the final total (i.e. including droplets of all sizes) concentration profile is shown in Fig. 8. The profiles were normalized with the respective final core-average total concentrations which are listed in Table 2. The plot resolution was $\Delta y^+ = 1.0$.

Fig. 8 focuses on the wall region where a considerable concentration buildup is observed. The degree of particle segregation, quantified by the maximum normalized concentration, $[\overline{C_t^f} / \langle C_t^f \rangle_{cr}]_{max}$, increases monotonically with increasing particle relaxation time. For $\tau^+ = 28$, the total concentration reaches a maximum value of about 5.5 its average value in the channel core within the limited evolution time of $t^+ = 100$. The maximum in the concentration profiles are located in the viscous sublayer ($y_{max}^+ \sim 1$–2). The concentration profiles are virtually uniform for $y^+ > 30$. Interdroplet collisions and coalescence can significantly affect the concentration profile. This is particularly true near the channel walls where the concentration reaches large values over time. Here, particle collisions can reduce the local concentration by roughly 50% relative to simulations of non-coalescing particles. Chen and McLaughlin (1995) showed that, if one integrates for a longer time, the maximum concentration continues to increase roughly in proportion to the time. They found that the particle concentration in the viscous wall region can be hundreds of times larger than the concentration in the channel core at $t^+ = 2000$.

Table 2 also shows the total final droplet concentrations in the channel core normalized with their initial concentration for various relaxation time constants. Only a slight decay of $\langle C_t \rangle_{cr}$ is observed, which justifies the assumption of a stationary droplet concentration in the core. The

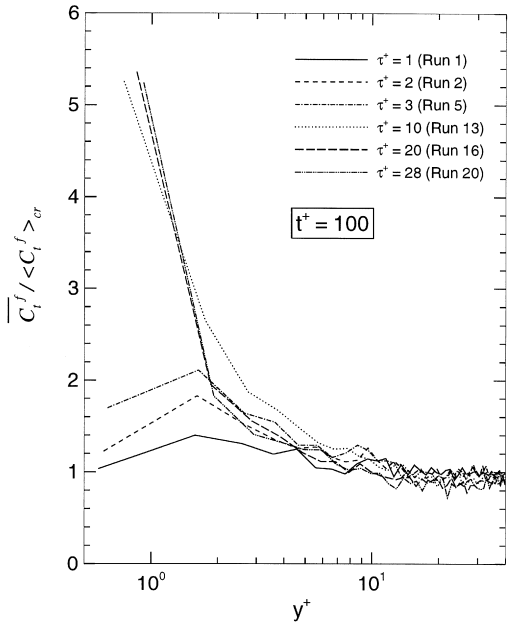

Fig. 8. Effect of droplet size (or, equivalently, of relaxation time) on average number concentration profiles at $t^+ = 100$ ($S = 713$; $Re = 7050$).

droplet concentration is reduced by dispersion to the wall regions of the channel and coalescence.

3.3.2. Micro-segregation

Even in homogeneous isotropic turbulence an initially uniform concentration distribution of droplets can develop small scale non-uniformities due to droplet inertia. Such micro-segregation phenomena have been discussed recently by Sundaram and Collins (1997) and Maxey (1987). In wall-bounded turbulence, the flow inhomogeneity has been known to result in a segregation of particles in elongated streaks in the vicinity of the wall. Particle trapping in the wall region of a channel flow has been observed by McLaughlin (1989) and Brooke et al. (1992).

Table 2
Total core averaged droplet concentrations at $t_f^+ = 100$ ($S = 713$)

Run ID	τ^+	C_0	$\langle C_t^f \rangle_{cr}$	$\langle C_t^f \rangle_{cr}/C_0$
1	1	3.78×10^5	3.72×10^5	0.985
2	2	3.78×10^5	3.69×10^5	0.975
5	3	3.78×10^5	3.58×10^5	0.946
13	10	2.52×10^5	2.23×10^5	0.885
16	20	1.26×10^5	1.07×10^5	0.849
20	28	6.30×10^4	5.42×10^4	0.860

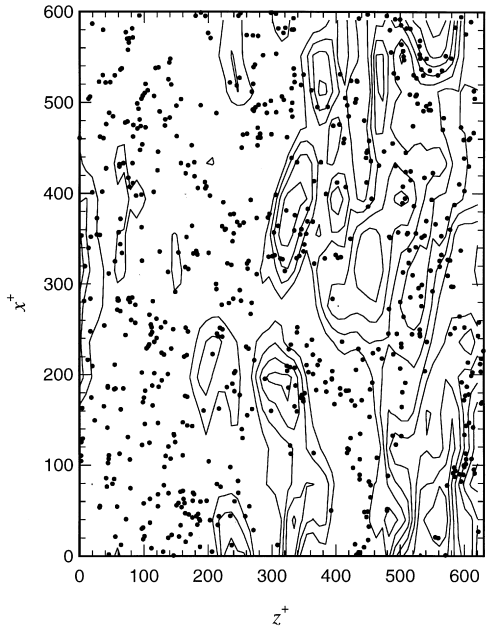

Fig. 9. Contours of low speed regions and distribution of droplets in the channel center (Run 16; $Y = 0$, $t^+ = 100$, $\tau^+ = 20$).

Figs. 9 and 10 show the locations of droplets found in the vicinity of two vertical x–z planes at $y_1^+ = 125$ (centerline) and $y_2^+ = 2.4$ (sublayer), respectively, at the end of Run 16. The contours of low speed regions at the same instant ($t^+ = 100$) on the two planes allow the association of the droplet distributions with the underlying turbulence kinematics. Particles with y^+ values within $(y_1^+ - \Delta y^+/2,\ y_1^+ + \Delta y^+/2)$ and $(y_2^+ - \Delta y^+/2,\ y_2^+ + \Delta y^+/2)$ are shown in Figs. 9 and 10, where $\Delta y^+ = 1.0$. Fig. 9 does not reveal any tendency of particles to accumulate in certain regions. It is possible that, if more particles were used, such tendencies might be revealed.

Fig. 10 indicates that the particles in the viscous sublayer concentrate in the low speed streaks. This is caused by the organized flow patterns in the viscous wall regions. Those particles residing in the viscous sublayer are brought away from the wall by bursts which have lower streamwise velocities than the sweeps. Chen (1995) discussed this phenomenon in detail. Such particle micro-segregation increases the local concentration to values that are even higher than those suggested by the maxima in the concentration profiles in Fig. 8.

Table 3 gives the fraction of droplets that are within five wall units of one of the channel walls at the end of the run for several cases. For droplets with $\tau^+ = 10$, about 10% of the droplets are within five wall units of one of the channel walls at the end of the run ($t^+ = 100$). This may be helpful in gauging the significance of wall phenomena to the overall evolution of the aerosols in the channel.

3.4. Droplet velocities

The mean streamwise droplet velocity profile determines the droplet residence times in the wall and core regions of the channel. Furthermore, according to Abrahamson's theory, the

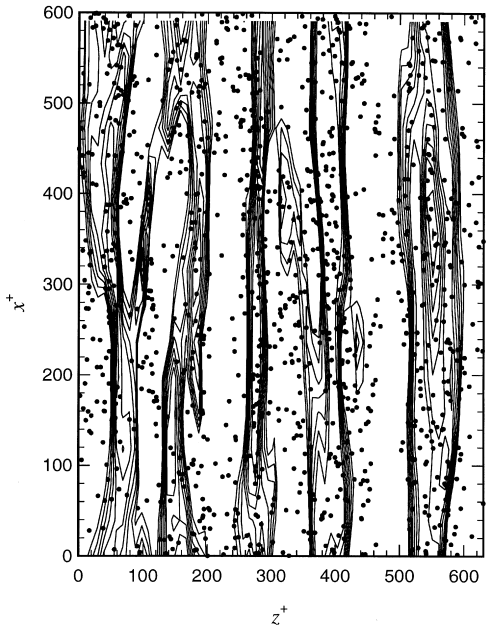

Fig. 10. The contours of low speed regions and the distribution of droplets in the viscous sublayer (Run 16; $Y = 122.6$, $t^+ = 100$, $\tau^+ = 20$).

interparticle collision rate in isotropic turbulence is proportional to the root-mean-square value of the particle velocity fluctuations. It is, therefore, of interest to examine at least the first and second order moments of the droplet velocities.

3.4.1. Mean velocities

Fig. 11 compares the mean streamwise velocity profiles for droplets with $S = 713$ and various relaxation times. The profile for the fluid, which can be viewed as the limit for $\tau^+ \to 0$, was also included for comparison. All profiles were normalized with the single-phase friction velocity, u^*. Mean velocities were computed at $t^+ = 100$ which ensures full entrainment of even the largest droplets considered. Mean velocities, averaged over all droplet sizes, were computed within bins of width $\Delta y^+ = 1$ centered at selected y^+ values.

Table 3
Fraction of droplets with $y^+ < 5$ at $t^+ = 100$ ($S = 713$)

Run ID	τ^+	Fraction with $y^+ < 5$
1	1	0.0490
2	2	0.0565
5	3	0.0644
13	10	0.0977
16	20	0.0891
20	28	0.0861

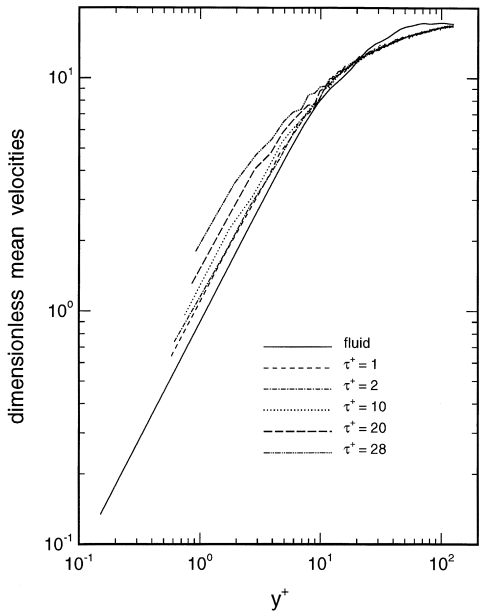

Fig. 11. Effect of relaxation time constant on droplet mean velocities ($S = 713$, $t^+\} = 100$, $\Delta y^+ = 1$).

The mean particle velocities in the core of the channel tend to be smaller than the corresponding fluid velocities. The same phenomenon has been seen in experiments by Kulick et al. (1994). It is a consequence of particle inertia and the mixing created by motion in the y-direction. Particles coming from regions closer to the wall tend to retain their original x-components of velocity, which are lower than the x-component of the fluid velocity in their current location. In the wall region, the opposite trend is observed; the x-component of the mean particle velocity is larger than the x-component of the mean fluid velocity. Once again, this is due to particle inertia. A consequence is that the mean particle velocity profile is flatter than the mean fluid velocity profile except very close the walls. This tendency is more pronounced for larger values of τ^+.

3.4.2. Velocity fluctuations

An appropriate velocity scale, $\sqrt{\overline{\overline{V^2}}}$, for application of the Abrahamson theory in the nearly isotropic channel core is obtained by averaging the rms particle velocity fluctuations over the three coordinate directions in the region $y^+ > 30$:

$$\sqrt{\overline{\overline{V^2}}} = \sqrt{\left(\frac{1}{3}(\langle\overline{V_x'^2}\rangle + \langle\overline{V_y'^2}\rangle + \langle\overline{V_z'^2}\rangle)\right)}. \tag{40}$$

Table 4 gives the dimensionless resulting $\sqrt{\overline{\overline{V^2}}}$ values for particles of various τ^+, calculated at $t^+ = 100$. The average fluid intensity in the core, $\sqrt{\overline{\overline{U^2}}}$, was defined similarly.

The intensity of the particle velocity fluctuations at $t^+ = 100$ is lower than that of the fluid because the particles do not respond to all the fluid scales of motion due to their

Table 4
Root-mean-square particle velocity fluctuations averaged over the three channel directions and over the channel core region at $t^+ = 100$

RUN ID	τ^+	$\sqrt{\overline{V^{+2}}}$	$\sqrt{\overline{V^{+2}}}/\sqrt{\overline{U^{+2}}}$
	0	0.964	1
1	1	0.955	0.991
2	2	0.953	0.989
5	3	0.948	0.984
13	10	0.895	0.929
16	20	0.847	0.879
20	28	0.819	0.850

inertia. The deviations between the particle and fluid fluctuation intensity increases with τ^+. The maximum deviation observed for droplets with $\tau^+ = 28$ was 15%. Furthermore, the initial particle velocity intensity at $t^+ = 0$ has to coincide with that of the fluid because the particles are released isokinetically. Therefore, the particle intensity varies only slightly over the duration of the simulations ($t^+ = 100$) as the particles respond to the fluctuations of the surrounding fluid. Therefore, the fluid intensity, $\sqrt{\overline{U^2}}$, which is generally more easily obtained, will be used for the interpretation of the observed collision rates in the core. The discrepancies between the particle and fluid velocities become more pronounced in the wall region. Fig. 12 shows the profiles for $\sqrt{\overline{U^2}}$ and $\sqrt{\overline{V^2}}$ for particles with $\tau^+ = 28$ which exhibited the largest

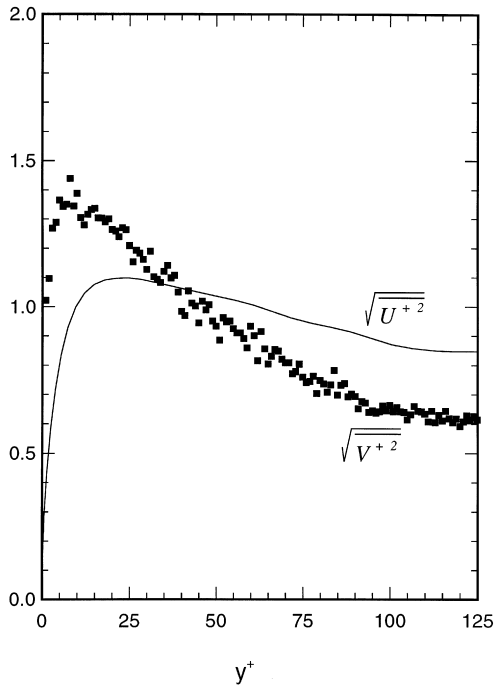

Fig. 12. Conditionally averaged RMS velocities of $\tau^+ = 28$ droplets and the fluid ($t^+ = 100$).

discrepancies. Fig. 12 shows that the difference between $\sqrt{\overline{U^2}}$ and $\sqrt{\overline{V^2}}$ is small except in the wall region.

3.5. Inter-droplet collisions

Interdroplet collisions are of particular interest because they lead to droplet coalescence and growth. Fig. 13 shows the dependence of the average droplet collision rate profile on droplet size for droplets with a density ratio, S, equal to 713 (olive oil in air) in a low Reynolds number channel flow (Re = 7050). Varying the droplet size at a constant density ratio is equivalent to varying the droplet relaxation time constant, τ, or the Stokes number defined as $St = \tau/\tau_k$, where τ_k is the time scale of the surrounding Kolmogorov eddies. Results at two different initial number concentrations are presented. The number concentration is preferred as an independent variable instead of the droplet volume fraction because of its direct influence on the collision rate as shown in the theory section.

The local time-averaged collision rate shown in Fig. 13, $Z(y^+)$, was calculated as

$$Z(y^+) = \frac{N_c}{(t_2^+ - t_1^+)\Delta V^+ t^* l^{*3}}, \tag{41}$$

where N_c is the total number of collisions between droplets of all sizes that occurred in a volume

$$\Delta V^+ = L_w^+ \Delta y^+ L_z^+ \tag{42}$$

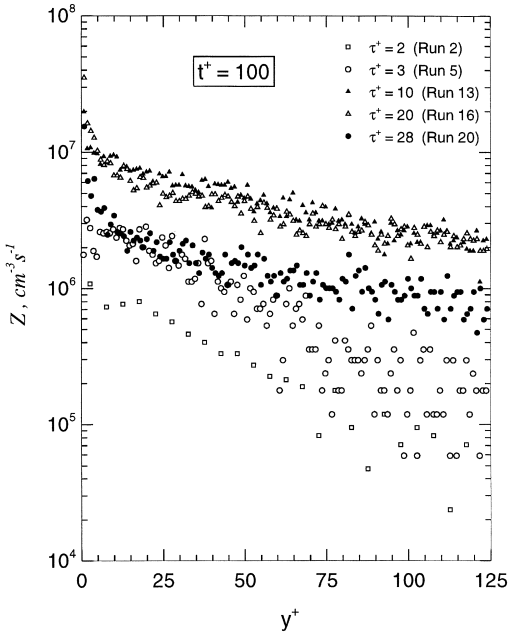

Fig. 13. Collision rates of droplets as a function of y^+.

centered around y^+ and $t_2^+ - t_1^+$ is the duration of the averaging. The value, $\Delta y^+ = 1$ is used in Fig. 13. The computed collision rates are independent of the time of release of the droplets, t_0, because the unladen channel flow was stationary. However, they depend, in principle, on the averaging time interval because the droplet behavior is evolving. The collision count was started at the time of release, $t_1^+ = t_0^+$, and was continued for 100 time wall units. Therefore, the duration of averaging even for the droplets with the largest relaxation time, $\tau^+ = 28$, was at least

$$t_2^+ - t_1^+ \geq 3\tau^+. \tag{43}$$

This constraint allowed sufficient time for particles to fully entrain into the surrounding flow. Including collisions before full droplet entrainment in the calculation of average collision rates introduces a small error. The width of the averaging volume, $\Delta y^+ = 1$, was sufficiently large to allow a statistically significant number of collisions over the observation time but small enough to resolve the variation of the average collision rate with distance from the wall.

Fig. 13 shows that the collision rate in the wall region is about an order of magnitude larger than in the channel core. This is probably due to the increase in the turbulence intensity and the previously discussed particle segregation in the wall region. Fig. 13 shows the range of variation in the average collision rate observed in this paper.

4. Interpretation of collision rates

The nearly homogeneous and isotropic flow conditions in the channel core allow the application of the collision theories reviewed in Section 2. The steep variation of turbulence properties and the continuous segregation of droplets, however, complicate the interpretation of collision rates in the wall region.

4.1. Channel core

It has been shown in the previous section that the turbulence intensities in the channel core, say $y^+ > 30$, are nearly homogeneous and isotropic. Furthermore, the average droplet concentration in the channel core remained almost constant and uniform over the limited observation time of $t^+ = 100$ and the suspension remained nearly monodisperse.

The stationarity of the collision rate in the core is illustrated in Fig. 14. Fig. 14 shows the evolution of the total number of collisions, $(N_c)_{cr,20}$, in the channel core occurring over successive time intervals of a fixed duration of 20 wall time units (i.e. 0–20, 20–40, 40–60, 60–80 and 80–100). Results are shown for droplets with $S = 713$ over a range of droplet sizes and initial concentrations.

Fig. 14 shows that droplets with small values of τ^+ reach a pseudo-stationary collision rate quickly. For droplets with larger values of τ^+, the collision rate changes significantly over the first 40 time wall units. This is because droplets with large values of τ^+ require more time to reach fully entrained states in a turbulent flow. After 40 time wall units, the collision rate decreases. This may be because of the slow decay of the droplet concentration in the channel

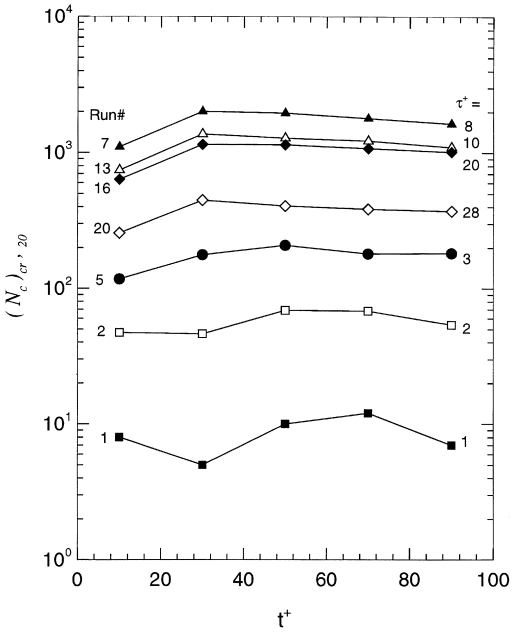

Fig. 14. Evolution of the total number of collisions occurring in the channel core during 20 wall time units.

core caused by deposition, accumulation near the walls, and coagulation. Fig. 14 shows that the collision rate is almost constant after 40 time wall units.

The observed collision rates are the result of a complex interplay of a number of factors.

4.1.1. Effect of droplet concentration

The dependence of the average collision rate in the channel core on the particle number concentration was systematically explored by varying the initial concentration, C_0, for particles of a given diameter and density (d = 16.8 μm or $d^+ = 0.84$, S = 713, $\tau^+ = 28$; Runs 19–22.) Fig. 15 shows the core values of the collision coefficients, $\langle z \rangle_{cr}$, calculated as

$$\langle z \rangle_{cr} = \frac{\Sigma_{y^+=30}^{y^+=h^+}(Z/C^2)\Delta y^+}{\Sigma_{y^+=30}^{y^+=h^+}\Delta y^+} \tag{44}$$

Here, $\Delta y^+ = 1$ was used. The particle number concentration in the core remained approximately constant over the averaging time interval, $t^+ = 0$–100.

The theories discussed in Section 2 assume that the suspension of particles or droplets is sufficiently dilute that virtually all collisions are binary. In this regime, the collision rate between equal sized droplets is expected to be proportional to the square of the particle concentration. Fig. 15 shows that z is independent of the droplet concentration.

4.1.2. Effect of droplet diameter

In the Saffman–Turner limit (very small τ^+), the collision coefficient is expected to have a cubic dependence on particle size. For larger particles, considered in this paper, the dependence

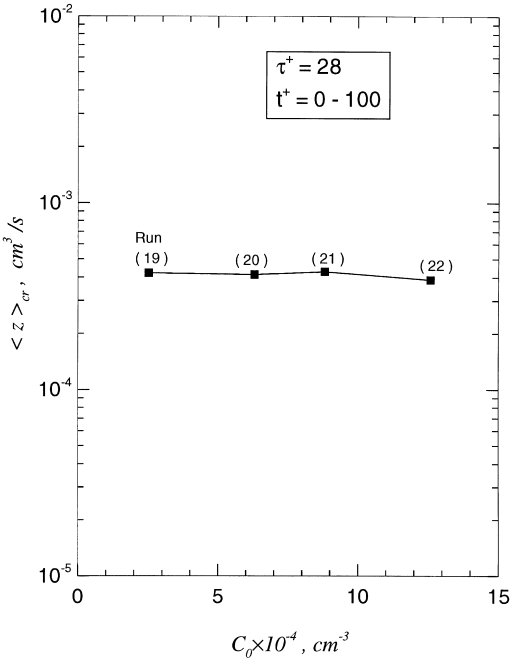

Fig. 15. Effect of olive oil droplet concentration on the collision coefficient ($S = 713$, $d^+ = 0.84$).

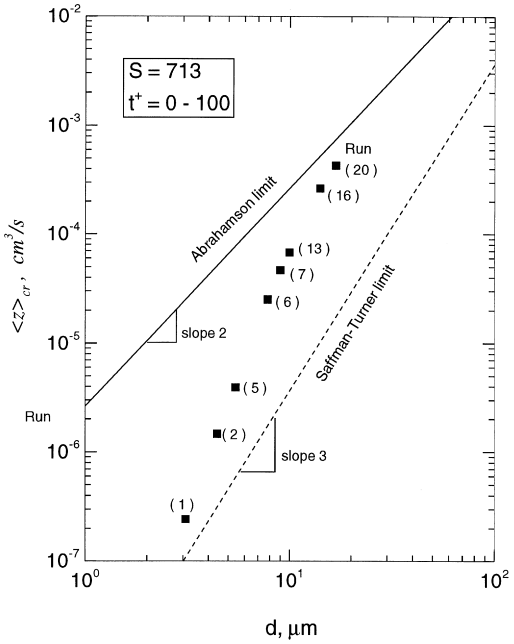

Fig. 16. Dependence of collision coefficient on the particle diameter ($S = 713$).

of the collision coefficient on the particle size is more complicated. Fig. 16 shows the collision coefficient as a function of the particle diameter. Only droplets with $S = 713$ are considered in Fig. 16. Only the collisions in the channel core ($y^+ > 30$) are considered. For comparison, results calculated from the Abrahamson theory and the Saffman–Turner theory are also plotted in Fig. 16.

The simulation results indicate that the droplets studied in this paper have a dependence on the droplet diameter stronger than the Abrahamson theory predicts. This dependence weakens as the droplet diameter increases. The smallest droplets approach the Saffman–Turner limit.

4.1.3. Effect of density ratio

Fig. 17 shows the collision coefficient as a function of the particle-fluid density ratio. Only the simulation results for a fixed particle diameter ($d = 9.96\ \mu$m) are presented. Fig. 17 shows that the density ratio significantly affects the collision coefficient.

The density ratio affects the collision rate because it affects the particle inertia. For a given size particle, its inertia increases as its density increases. Particles with little inertia follow the fluid motions well. In this regime, fluid shear is the main cause of the collisions. For the particle size (9.96 μm) in Fig. 17, Brownian motion is negligible. Particles with large inertia do not follow the fluid motions. In this regime, the turbulent intensity plays an important role in causing collisions.

When the density ratio is small enough ($\tau^+ \rightarrow 0$), the collision coefficient will be independent of the density ratio, according to Saffman and Turner (1956). Fig. 17 shows such a tendency.

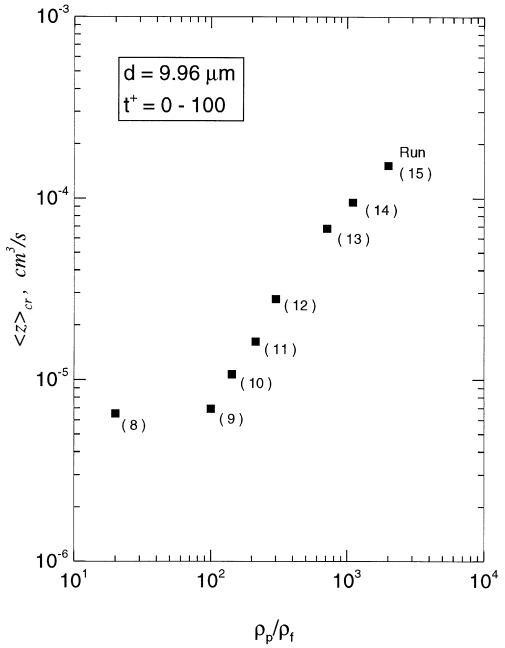

Fig. 17. Effect of particle–fluid density ratio on the collision coefficient.

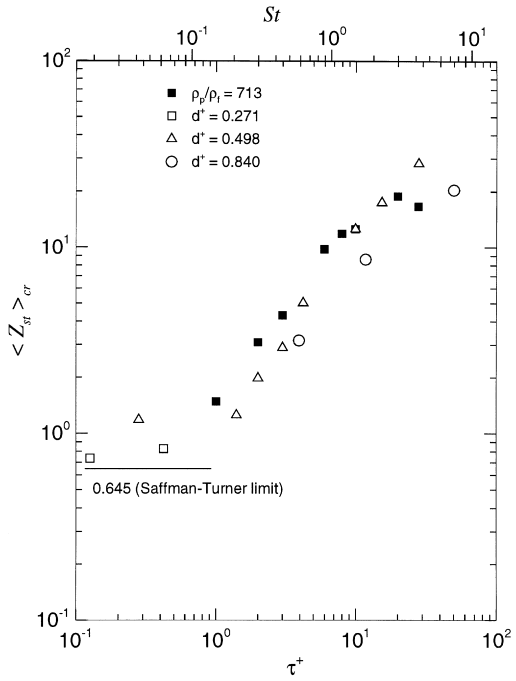

Fig. 18. Droplet collision rates normalized by the Saffman–Turner scaling as a function of τ^+.

4.1.4. Effect of droplet inertia: Saffman and Turner theory

According to ST, in the limit of particles with negligible inertia,

$$Z_{\mathrm{st}} = \frac{Z}{C^2 d^3 \sqrt{\epsilon/\nu}} = 0.65. \tag{45}$$

The range of applicability of the above limiting relationship is examined in Fig. 18.

Fig. 18 shows the dimensionless average collision rate, $\langle Z_{\mathrm{st}} \rangle_{\mathrm{cr}}$, in the channel core as a function of the droplet inertia quantified in terms of its dimensionless relaxation time, τ^+. The values of $\langle Z_{\mathrm{st}} \rangle_{\mathrm{cr}}$ were obtained by averaging Z_{st} over the region $y^+ > 30$ using the local values of $Z(y)$ and $\epsilon(y)$:

$$\langle Z_{\mathrm{st}} \rangle_{\mathrm{cr}} = \frac{\Sigma_{y=-(h^+-30)}^{y=h^+-30} Z_{\mathrm{st}} \Delta Y}{\Sigma_{Y=-(h^+-30)}^{Y=h^+-30} \Delta Y}, \tag{46}$$

where $\Delta Y = 1.0$. The variation of Z_{st} in the region $y^+ > 30$ was weaker than that of Z.

With the exception of the run for $\tau^+ = 50$, the concentrations at $t^+ = 100$ were used to normalize the collision rates. For the $\tau^+ = 50$ droplets, the run time was divided into six intervals of length 50 wall units each. A dimensionless collision rate was computed for each time interval using the concentration at the end of the interval in the normalizing factor. Finally, the overall collision rate was computed by averaging the values for the six intervals. The droplet relaxation time, τ^+, was varied by varying either the droplet size with constant droplet-gas density ratio or the density ratio at a fixed droplet size.

For comparison of collision results from different flows it may be more appropriate to quantify the particle inertia in terms of its Stokes number

$$St = \frac{\tau^+}{\tau_k^+}, \tag{47}$$

where τ_k^+ is the Kolmogorov time scale of the eddies that drive the particle motion. In channel flow, the Kolmogorov time scale and, therefore, the Stokes number vary with distance from the closest channel wall. However, in the channel core, they can both be assumed approximately homogeneous. Furthermore, since all the results in this paper were obtained from the same channel flow simulation, the St numbers for different type droplets in the channel core become directly proportional to their relaxation time constants. Turbulence in the core was characterized by a single value for the Kolmogorov time scale, calculated as $\tau_k^+ = 1/\sqrt{+}$. The dimensionless dissipation rate, $\epsilon^+ = \epsilon/\epsilon^*$, where $\epsilon^* = u^{*4}/\nu$ was estimated from Fig. 2. An average value of $\epsilon_{cr}^+ \approx 0.0226$ in the channel core leads to $\tau_{k,cr}^+ = 6.65$.

Fig. 18 suggests that $\langle Z_{st}\rangle_{cr}$ is primarily a function of τ^+ in the range of conditions covered. However, some remaining variation in the computed $\langle Z_{st}\rangle_{cr}$ values should be attributed to independent effects of S and d^+, not captured by the effect of τ^+ and to statistical scatter due to the limited number of computed collisions. The statistical error increases at the smaller τ^+ values. This is shown in Table 5 where the central limit theorem is used to estimate the statistical uncertainty in the core-averaged collision rates.

According to ST, $\langle Z_{st}\rangle_{cr}$ should become independent of S and d^+ (and, therefore, τ^+) in the limit of $\tau^+ \to 0$. Indeed, Fig. 18 seems to be consistent with this expectation for $\tau^+ < 1$. The computed average value of $\langle Z_{st}\rangle$ for $\tau^+ < 1$ is 0.914. The value expected from the theory of ST (0.65) is 28% lower. In addition to particle inertia effects, due to non-zero values of τ^+, and statistical errors, this discrepancy could be attributed to a number of factors. First, ST did not consider the presence of a mean shear which could be contributing to the computed collision rates in channel flow. Furthermore, ST assumed that the fluid shear rate was normally distributed which is only approximately correct even in homogeneous turbulence. Moreover, a small Brownian contribution, not accounted for by ST, could be slightly enhancing the computed collision rates for $\tau^+ < 1$. Finally, the small degree of polydispersity could be enhancing the computed collision rates by contributing collisions between neighboring particles being accelerated at different rates.

4.1.5. Effect of droplet inertia: Abrahamson theory

According to the theory of Abrahamson, in the limit of particles with very large inertia,

$$Z_a = \frac{Z}{C^2 d^2 \sqrt{V^2}} = 3.54. \tag{48}$$

Since $\overline{U^2}$ is easier to obtain than $\overline{V^2}$, a modified Abrahamson scaling is defined as

$$Z_{ma} = \frac{Z}{C^2 d^2 \sqrt{U^2}}. \tag{49}$$

Table 5
Statistical uncertainty in core-averaged collision rates

Run ID	τ^+	$(N_c)_{cr}$	$\frac{1}{\sqrt{(N_c)_{cr}}}$
1	1.0	42	0.15
2	2.0	284	0.059
3	0.126	67	0.12
4	0.421	80	0.11
5	3.0	864	0.034
6	6.0	6104	0.013
7	8.0	8498	0.011
8	0.280	427	0.048
9	1.402	164	0.078
10	2.0	245	0.064
11	3.0	439	0.048
12	4.2	649	0.039
13	10.0	5709	0.013
14	15.4	501	0.045
15	28.0	797	0.035
16	20.0	5011	0.014
17	4.0	353	0.053
18	12.0	964	0.032
19	28.0	305	0.057
20	28.0	1862	0.023
21	28.0	3797	0.016
22	28.0	7015	0.012
23	50.0	6531	0.012

For the range of conditions examined in this paper, $\overline{V^2} \approx \overline{U^2} \approx 0.964u^*$ for $y^+ > 30$ (see Table 4). Therefore, the difference between Z_a and Z_{ma} should be small.

Fig. 19 shows the dimensionless collision rate, $\langle Z_{ma} \rangle_{cr}$, in the channel core ($y^+ > 30$) as a function of particle inertia quantified in terms of its relaxation time, τ^+, and Stokes number, St. The values of $\langle Z_{ma} \rangle_{cr}$ were obtained by averaging Z_{ma} over the region $y^+ > 30$ using the local values of $Z(y)$, $C(y)$ and $\sqrt{U^2}$:

$$\langle Z_{ma} \rangle_{cr} = \frac{\Sigma_{Y=-(h^+-30)}^{Y=h^+-30} Z_{ma} \Delta Y}{\Sigma_{Y=-(h^+-30)}^{Y=h^+-30} \Delta Y}, \tag{50}$$

where $\Delta Y = 1.0$ is used. For $y^+ > 30$, Z_{ma} does not vary significantly with y^+.

With the exception of the run for $\tau^+ = 50$, the concentrations at $t^+ = 100$ were used to normalize the collision rates. For the $\tau^+ = 50$ droplets, the run time was divided into six intervals of length 50 time wall units each. A dimensionless collision rate was computed for each time interval using the concentration at the end of the interval in the normalizing factor. Finally, the overall collision rate was computed by averaging the values for the six intervals.

Fig. 19 shows that, for $\tau^+ > 3$, $\langle Z_{ma} \rangle_{cr}$ becomes a monotonically increasing function of τ^+ alone. No independent effect of S or d^+ can be detected within the statistical accuracy of the

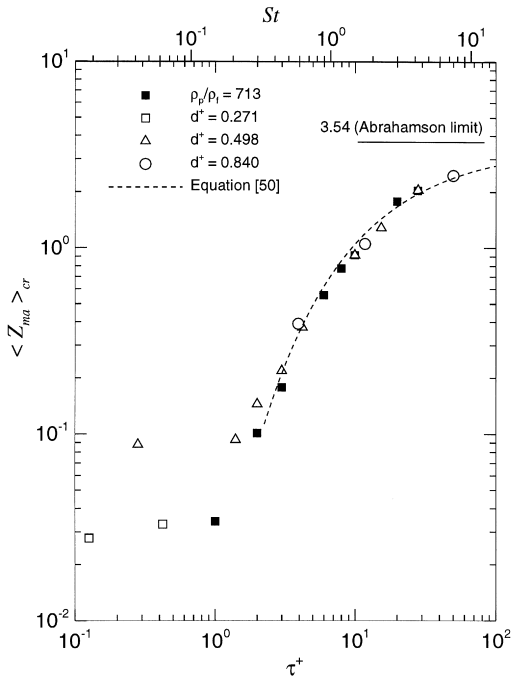

Fig. 19. Droplet collision rates normalized by the modified Abrahamson scaling as a function of τ^+.

points in Fig. 19. The following expression can be used as an approximation to $\langle Z_{\mathrm{ma}}\rangle_{\mathrm{cr}}$:

$$\langle Z_{\mathrm{ma}}\rangle_{\mathrm{cr}} = 3.54\exp[-6.05(\tau^+)^{-0.695}], \quad \tau^+ \geq 3. \tag{51}$$

When $\tau^+ < 3$, the variation of Z_{ma} cannot be explained solely in terms of τ^+. The exclusive dependence of the collision rate on τ^+ suggests that over the range of conditions and particle sizes considered in this paper, droplet inertia is the dominant collision mechanism. Inertia plays a key role in the collisions of even small particles, which follow the fluid to a good approximation and are brought close to one another by fluid shear, because it causes their actual impact.

4.2. Wall region

The interpretation of collision rates in the vicinity of the wall is complicated by a number of factors. First, turbulence properties (e.g. intensities and dissipation rate) vary strongly with the distance from the wall. Moreover, the droplet concentration profile exhibits a continuous buildup in the viscous wall region and significant microstructure. Since the collision rate is proportional to C^2, the collision and coalescence rate in the wall region can be much larger than in the channel core. Consequently, larger deviations from monodispersity are expected. There is no established theory for the collision rate in polydisperse suspensions of non-uniform and non-stationary concentrations in inhomogeneous, anisotropic turbulence.

Fig. 20 shows the average collision coefficient profiles, $z(y^+)$, for droplets with $S = 713$ and various sizes. To calculate $z(y^+)$, the channel was divided into a number of bins. The bin width

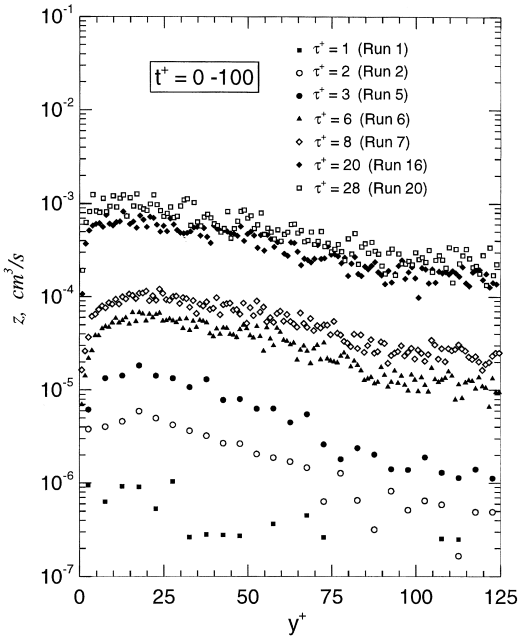

Fig. 20. Collision coefficient profiles for droplets of various sizes ($S = 713$).

for droplets of $\tau^+ \geq 6$ is 1 wall unit. The bin width for droplets of $\tau^+ \leq 3$ is 5 wall units. In each bin, the collision rate (Z) and the droplet number concentration (C) at the end of run ($t^+ = 100$) were calculated. Based on Z and C, $z(y^+)$ is obtained by

$$z(y^+) = \frac{Z}{C^2}. \tag{52}$$

A comparison with Fig. 13 in Section 3.5 shows that the increase in the collision rate in the vicinity of the walls can be at least partly attributed to the direct effect of the increased average droplet concentration. The rate of change of z with τ^+ appears to be diminishing at large τ^+. This is consistent with the computation of Sundaram and Collins (1997) which showed a maximum at $St \approx 4$.

Some of the remaining variation in the collision coefficient with distance from the wall may be accounted for by the inhomogeneity in the turbulence properties. Figs. 21 and 22 show the collision rate profiles for droplets with $S = 713$ normalized with the ST scaling($C^2 d^3 \sqrt{/v}$)and the modified Abrahamson scaling($C^2 d^2 \overline{U^2}$), respectively. The simulation time was 100 time wall units. The concentration at the end of the run was used to normalize the collision rate. To obtain Z_{st} and Z_{ma}, the channel was divided into a number of bins in the direction normal to the walls. The bin width was 1.0 wall units for the droplets with $\tau^+ \geq 6$. For droplets with $\tau^+ \leq 3$, the bin width was 5.0 wall units.

For droplets with $\tau^+ \leq 3$, Figs. 21 and 22 suggest that neither the ST nor the modified Abrahamson scaling can adequately explain the variation of the collision rate with distance from the wall. The dimensionless collision rates, Z_{st} and Z_{ma}, show a significant dependence on y^+. For droplets with $\tau^+ > 6$, Figs. 21 and 22 suggest that both the ST and the modified

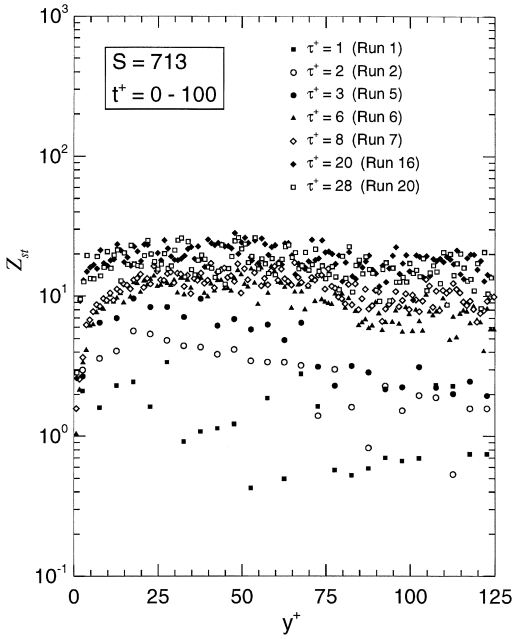

Fig. 21. Droplet collision rate profiles normalized by the Saffman–Turner scaling ($S = 713$).

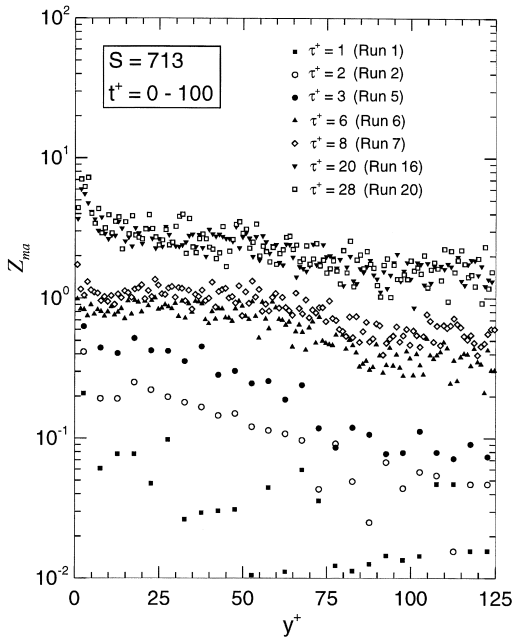

Fig. 22. Droplet collision rate profiles normalized by the modified Abrahamson scaling ($S = 713$).

Abrahamson scaling can adequately explain the variation of the collision rate with distance from the wall except the wall region. The ST scaling makes the normalized collision rate more independent of y^+ than the modified Abrahamson scaling even though the ST theory is only applicable to small inertia particles. On the other hand, the Abrahamson theory was developed for large inertia particles in homogeneous turbulence. Since the droplets covered in this paper do show particle–fluid velocity correlations (see Table 4), the particle inertia may not be large enough to adequately apply the Abrahamson theory. Moreover, since the flow Reynolds number of the numerical channel used in this work was only 7050, the requirement of homogeneous turbulence may not be met.

Figs. 21 and 22 suggest that the Abrahamson scaling captures the inhomogeneity effects for droplets with large values of τ^+ and the Saffman–Turner scaling is appropriate for droplets with small values of τ^+. The transition between the two regimes occurs between τ^+ roughly equal to 1 and τ^+ roughly equal to 3. In this regime, the collision rate normalized with either the Abrahamson scaling or the Saffman–Turner scaling still shows a significant dependence on y^+.

5. Conclusion

Part II of this paper presented inter-droplet collision rates in the channel core and wall regions. Over the range of conditions and particle sizes considered, droplet inertia was the dominant mechanism for collisions. A significant result was the variation of the collision rate with droplet inertia in the channel core for a fixed Reynolds number, shown in Figs. 18 and 19. The Saffman–Turner theory was found to be in reasonable agreement with the DNS results for droplets with relaxation time constants $\tau^+ < 1$ (or equivalently $St < 0.15$). For $3 < \tau^+ < 50$ (or $0.45 < St < 7.5$), the collision rate scaled as suggested by the theory of Abrahamson becomes a function of τ^+ alone. It appears that the Kolmogorov time scale and the friction velocity define the transition between the Saffman–Turner and the Abrahamson regimes. This suggests that the transition value of τ^+ is a weak function of the Reynolds number. In none of the cases considered in this paper did Brownian motion or gravity influence the results significantly.

This paper did not examine the coupling between Brownian and turbulence-driven collisions. Moreover, the range of conditions examined did not reach the limit of high particle inertia where the Abrahamson theory may be applicable. Extension of this work to smaller and larger particle inertia would therefore be useful. Further work is also needed to identify the scales of motion that contribute to the collision rates and explore the dependence of the average collision rate on the flow Reynolds number.

All the runs that were reported in this paper were performed for a single channel Reynolds number. Thus, it is not possible to draw a conclusion regarding the question of how dimensionless collision rates scale with Reynolds number. Within the context of the present runs, the most important parameter is the dimensionless particle relaxation time, τ^+. The particle-fluid density ratio, S, had little influence on the dimensionless collision rates. However, the runs were performed for a regime in which Brownian collisions were relatively unimportant (although this was not obvious *a priori* for the smallest particles). For smaller friction

velocities, one might expect the smallest particles to be more strongly affected by Brownian motion.

Acknowledgements

The authors wish to acknowledge the support and facilities of the National Center for Supercomputing Applications at the University of Illinois at Urbana. The authors also acknowledge financial support for this project by DuPont and Clarkson's Center for Advanced Materials Processing (CAMP). This material is based upon work supported in part by the New York State Science and Technology Foundation. Many of the techniques used in this work were developed with previous support from Dr Robert Price's program at the United States Department of Energy under contract DE-FG02-88ER13919.

Appendix A

The result for the collision rate of small particles in a homogeneous turbulent flow in Eq. (10) may be found in Eq. (1) of Saffman and Turner's (1954) paper. Typographical errors in the latter paper have lead to some confusion in the past. Therefore, the result will be derived in this appendix and the errors in ST will be identified. ST assume that the spatial derivative, $f = \partial u/\partial x$ is normally distributed. Thus, the mean square value of f is given by

$$\overline{f^2} = \int_0^\infty f^2 \mathrm{e}^{-f^2 q^2} \mathrm{d}f / \int_0^\infty \mathrm{e}^{-f^2 q^2} \mathrm{d}f. \tag{A1}$$

The values of the numerator and denominator in (A1) are $\sqrt{\pi/4q^3}$ and $\sqrt{\pi/2q}$, respectively. Thus,

$$\overline{f^2} = \frac{1}{2q^2}. \tag{A2}$$

It follows from Eq. (8) and (A1) that

$$q = \left(\frac{15\nu}{2\epsilon}\right)^{1/2}. \tag{A3}$$

To derive the result in Eq. (9), let us compute $\bar{f}$:

$$\bar{f} = \int_0^\infty f \mathrm{e}^{-f^2 q^2} \mathrm{d}f / \int_0^\infty \mathrm{e}^{-f^2 q^2} \mathrm{d}\bar{f}. \tag{A4}$$

The values of the integrals in the numerator and denominator of eqn (A4) are $1/2q^2$ and $\sqrt{\pi/2q}$, respectively. Thus,

$$\bar{f} = \frac{1}{\sqrt{\pi} q}. \tag{A5}$$

Using the expression for q in eqn (A3), one obtains the expression for $\bar{f}$ in Eq. (9). From

Saffman and Turner's paper,

$$N = n_1 n_2 R^3 (2\pi)\left(\frac{2\epsilon}{15\pi v}\right)^{1/2} = n_1 n_2 R^3 \left(\frac{8\pi\epsilon}{15v}\right)^{1/2}. \tag{A6}$$

Therefore, Eq. (1) in Saffman and Turner's paper is correct even though the expression for $\overline{\partial u/\partial x}$ above it is incorrect.

References

Abrahamson, J., 1975. Collision rates of small particles in a vigorously turbulent fluid. Chemical Engineering Science 30, 1371–1379.

Beal, S.K., 1972. Turbulent agglomeration of suspensions. Aerosol Science 3, 113–125.

Brooke, J.W., Kontomaris, K., McLaughlin, J.B., 1992. Turbulent deposition and trapping of aerosols at a wall. Physics of Fluids A 4, 825–834.

Chen, M., 1995. Aerosol deposition, dispersion and interaction in turbulent channel flows. Ph.D. thesis. Clarkson University, Potsdam, NY.

Chen, M., McLaughlin, J.B., 1995. A new correlation for the aerosol deposition rate in vertical ducts. Journal of Colloid Interface Science 169, 437–455.

Hu, C., Mei, R., 1997. Effect of inertia on the particle collision coefficient in Gaussian turbulence. Seventh International Symposium on Gas-Particle Flows, Vancouver. .

Kim, J., Moin, P., Moser, R., 1987. Turbulence statistics in fully developed channel flow at low Reynolds number. Journal of Fluid Mechanics 177, 133–166.

Kontomaris, K., Hanratty, T.J., 1994. Effect of molecular diffusivity on point source diffusion in the center of a numerically simulated turbulent channel flow. International Journal of Heat and Mass Transfer 37, 1817–1828.

Kulick, J.D., Fessler, J.R., Eaton, J.K., 1994. Particle response and turbulence modification in fully developed channel flow. Journal of Fluid Mechanics 277, 109–134.

Lyons, S.L., Hanratty, T.J., McLaughlin, J.B., 1991. Large-scale computer simulation of fully developed channel flow with heat transfer. International Journal of Numerical Methods of Fluids 13, 999–1028.

Maxey, M.R., 1987. The gravitational settling of aerosol particles in randomly oriented cellular flow fields. Journal of Fluid Mechanics 174, 441–465.

McLaughlin, J.B., 1989. Aerosol particle deposition in numerically simulated channel flow. Physics of Fluids A 1, 1211–1224.

Saffman, P.G., Turner, J.S., 1956. On the collision of droplets in turbulent clouds. Journal of Fluid Mechics 1, 16–30.

Sundaram, S., Collins, L.R., 1997. Collision statistics in an isotropic particle-laden turbulent suspension. Part I. Numerical simulations. Journal of Fluid Mechanics 335, 75–109.

Williams, J.J., Crane, R.I., 1983. Particle collision rate in turbulent flow. International Journal of Multiphase Flow 9, 421–435.